CURE-INDUCED VISCOELASTIC EFFECTS IN IN-AIR PHOTOPOLYMERIZED DROPLETS FOR MICROFLUIDIC DROPLET-BASED 3D PRINTING

Saquib Rouf[1], **Johnny Moughames**[1], **Arnaud Bertsch**[2], **H. Jerry Qi**[3], **and Frédéric Demoly**[1,4*]

[1] Université Marie et Louis Pasteur, UTBM, CNRS, ICB UMR 6303, Belfort, France
[2] Microsystems Laboratory, EPFL, Lausanne, Switzerland
[3] Georgia Institute of Technology, Atlanta, USA
[4] Institut universitaire de France (IUF), Paris, France

April 29, 2026

ABSTRACT

Motivated by droplet-based additive manufacturing processes, this work presents a multiphysics numerical framework for in-air photopolymerization of resin droplets and their subsequent impact, spreading, and recoil on a solid substrate. The model couples two-phase compressible flow with energy and species transport, incorporating radiative transport through the Beer-Lambert law to describe free-radical photopolymerization. This formulation enables prediction of core-shell droplet morphologies, in which a partially or fully cured outer shell encapsulates an uncured liquid core prior to impact. The key novelty of the proposed framework lies in the introduction of a cure-induced viscoelastic shell model, described using an Oldroyd-B-type constitutive formulation. The evolving stress response during photocuring is decomposed into equilibrium (elastic, spring-like) and non-equilibrium (viscous, Maxwell-type) contributions. The viscoelastic properties of the shell – including relaxation time as well as equilibrium and non-equilibrium moduli – are explicitly linked to the local degree of cure, allowing the progressive evolution of material stiffness and elasticity to be captured. Using this approach, we systematically quantify how cure-dependent viscoelasticity governs droplet-substrate interaction for micron-scale droplets across a range of shell thicknesses, degrees of cure, and impact velocities. Particular emphasis is placed on the role of viscoelasticity in post-impact recoil and rebound suppression. The proposed model provides a predictive tool for understanding and controlling droplet dynamics in UV-curable, droplet-based additive manufacturing processes.

***K*eywords** Microdroplet · Photopolymerization · Viscoelasticity · Numerical modeling · 3D printing

1 Introduction

Droplet dynamics play a central role in additive manufacturing, especially in material jetting (Feng et al., 2024; Wang et al., 2024; Gilani et al., 2023), drop-on-demand printing (Hu et al., 2022; Khalil et al., 2025; Karakaya et al., 2022), continuous inkjet printing, aerosol jet printing (Seiti et al., 2023; Zeng et al., 2023; Vlnieska et al., 2022; Ramesh et al., 2022), electrohydrodynamic jet printing (Mkhize and Bhaskaran, 2022; Im et al., 2023), binder jetting, and microfluidic droplet-based printing (Lee et al., 2026; Zhang et al., 2024). The latter encompass existing 3D printing technologies in which discrete liquid droplets are generated, transported, and deposited to build three-dimensional structures through controlled solidification mechanisms. In these 3D printing techniques, resin droplets are deposited onto a substrate, where their impact, spreading, and solidification govern the fidelity of printed features and directly influence the quality of subsequent layers (Layani et al., 2018; Ligon et al., 2017; Stansbury and Idacavage, 2016). A precise understanding

*Corresponding author: frederic.demoly@utbm.fr

and control of droplet solidification and droplet-substrate interaction are therefore needed for achieving accurate and repeatable 3D-printed structures.

A previous study has investigated the spreading behavior of static droplet on a thermo-active substrate; however, their study neglected the coupled effects of chemical reaction and thermal evolution occurring during in situ curing (De Ruiter et al., 2018). To address this limitation, subsequent research explored droplet spreading accompanied by photopolymerization on the substrate (Sivasankar et al., 2020), and later extended this work to study droplet impingement dynamics (Bera et al., 2025). In these studies, the evolving rheology of the polymer was modeled using cure-dependent shear-thinning viscosity laws. While such approaches represent curing primarily through viscosity (and sometimes density) evolution, they weakly represent the emergence of elastic stresses and time-dependent relaxation during network formation, which are often required to match experimental mechanical responses (Sivasankar et al., 2020; Bera et al., 2025). Droplets undergoing simultaneous curing and impact exhibit cure-induced viscoelastic behavior, which plays a crucial role in governing impact dynamics. Viscoelasticity describes the time-dependent mechanical response of materials that exhibit both viscous dissipation and elastic energy storage under deformation (Cohen et al., 1998). Materials with viscoelastic properties typically behave elastically at short timescales and viscously at longer timescales, i.e., a distinction relevant in transient processes such as droplet impingement. The rheology of material plays an important role on the droplet dynamics. This can be understood by a simple example of adding polyethylene oxide in water that suppresses the rebound which is attributed to enhanced extensional viscosity due to flexible polymer chains. These polymer chains provide viscous resistance towards retraction and hence damping the rebound (Bergeron et al., 2000).

Similar studies conducted on hydrogel droplets suggest that upon tuning the elastic modulus of hydrogel, an intermediate configuration emerges between wetting and contact (Kim et al., 2024; Chakrabarti et al., 2018). The spreading characteristics of weakly elastic droplet can be linked with Newtonian drop (pure wetting) while as for highly elastic drop, a solid-like response (non-wetting) is observed (Kim et al., 2024). Prior literature in droplet-substrate interaction focused on spreading dynamics of droplets whose shear storage modulus, was smaller than the shear loss modulus (Bouillant et al., 2022; Yada et al., 2023; Varma et al., 2020). There, spreading dynamics is dominated by viscosity or inertia, therefore a drop behaves like Newtonian fluid or a weakly elastic polymer. The role of a non-trivial, elastic modulus remains unexplored. To bridge this gap, researchers worked on polyacrylamide droplet, whose Young's modulus range from 0.16 kPa to 366 kPa (Mitra et al., 2026). They categorized the droplet-substrate interaction in two regimes: an early viscous regime, where capillary-driven spreading is governed by viscous dissipation, with polymer chains effectively unrelaxed (behaving Maxwell-fluid like); and an elasto-capillary regime, that arises when the spreading timescale is shorter than the viscoelastic relaxation time. In the elasto-capillary regime, the contact line decelerates sharply, therefore exhibiting oscillations (interpreted by standard linear model of viscoelasticity) (Mitra et al., 2026). Importantly, when no dynamic effects are present, their model simplifies to the Johnson-Kendall-Roberts (JKR) theory describing elastic contact at equilibrium. This approach provides a unified description of wetting and contact mechanics, which is useful for bioprinting, where resolution is related to the interplay between viscoelasticity and contact line motion. To model the viscoelastic fluids, researchers have extensively used the Oldroyd-B, FENE-P, and Maxwel models (Bird et al., 1986; Alves et al., 2021). In these models, viscoelasticity is represented using rheological elements that combine an elastic spring and a viscous dashpot. The specific series/parallel arrangement defines the chosen constitutive law (e.g., Maxwell, generalized Maxwell, or standard linear solid). For the viscoelastic shell, a generalized Maxwell model is adopted, where the relaxation behavior is represented by n Maxwell branches. The n-th branch consists of a spring with modulus (E_n) in series with dashpot of viscosity (η_n), defining a relaxation time ($\lambda_n = \eta_n/E_n$). The elastic modulus governs the magnitude of recoverable stress under deformation, whereas the relaxation time sets the timescale over which these stresses relax. Assuming isotropy with a constant Poisson's ratio ν, the corresponding shear modulus is $G_n = E_n/[2(1+\nu)]$. It must be noted that the polymeric viscosity is a derived quantity, not an independent parameter. Considering viscoelastic droplets, polymeric viscosity introduces strain rates that dissipate some part of the energy within the system. The relaxation time is defined as the time required for the viscoelastic droplet to reach its equilibrium state. In other words, it determines how long the stresses take to relax (Zhao et al., 2024). In viscoelastic fluid models, a purely elastic solid can be obtained at the limit where the relaxation time tends to infinity, while maintaining a constant shear modulus (Snoeijer et al., 2020).

The influence of viscoelasticity on droplet impact phenomena has also been extensively studied. Prior works have shown that viscoelastic effects can significantly alter droplet deformation, spreading, bouncing, and splashing behavior, and have highlighted transitions between elastic-dominant and shear-thinning regimes (Wang et al., 2017). The role of viscoelasticity has also been examined through dimensionless parameters such as the Reynolds number, where increasing inertia amplifies viscoelastic effects during spreading, therefore rendering the dynamics increasingly independent of the equilibrium contact angle (Venkatesan and Ganesan, 2019). During the rebound phase, viscoelastic stresses generate resistance against surface tension forces, therefore affecting the contact-line and damping the rebound phenomena (Bartolo et al., 2007). Interestingly, several studies have demonstrated that viscoelasticity does not significantly affect

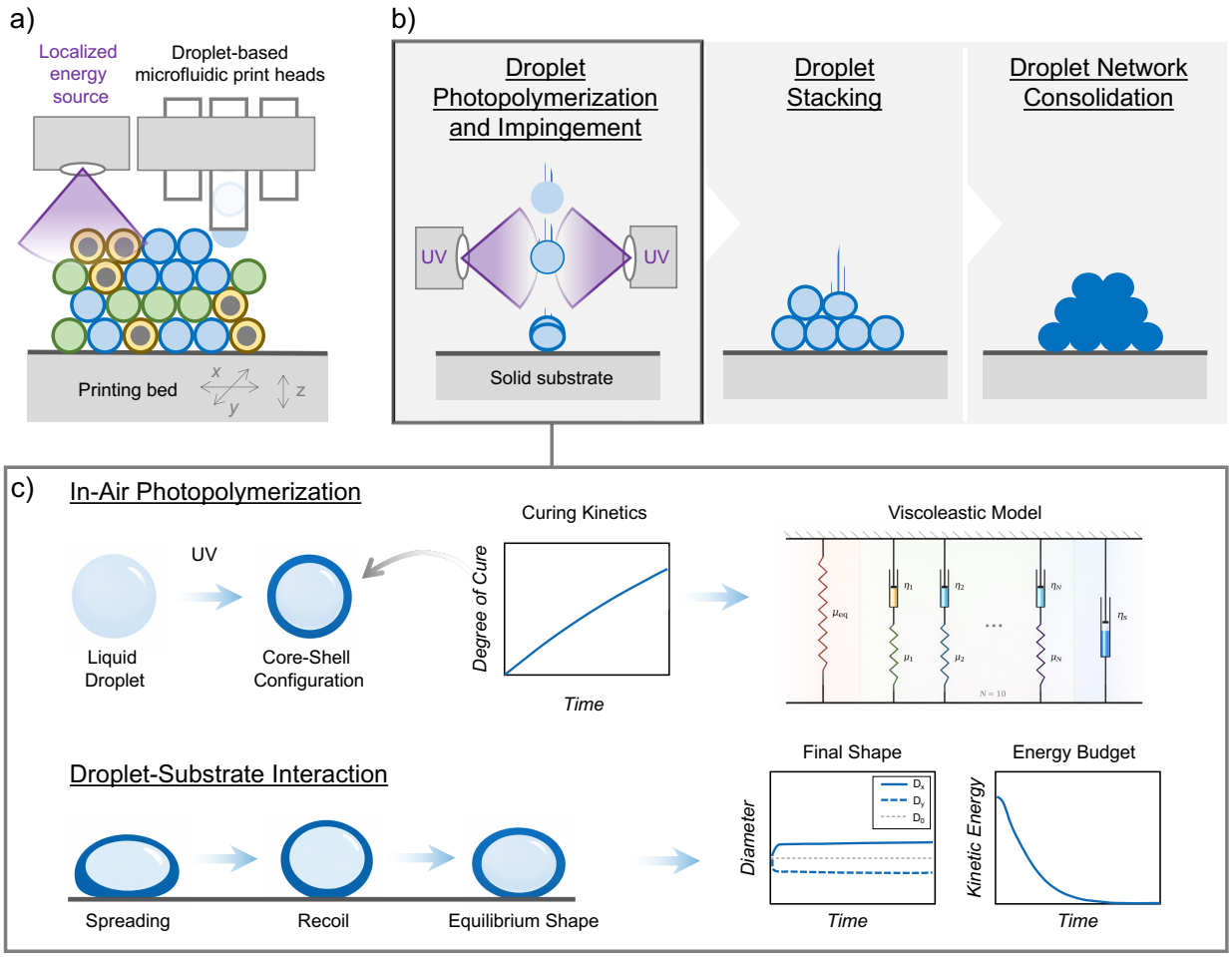

Figure 1: Microfluidic droplet-based 3D printing: (a) Schematic of the printing technique; (b) process steps covering droplet photopolymerization and impingement, droplet stacking, and droplet network consolidation, where four UV sources are positioned at 90° intervals in the z-plane; and (c) droplet photopolymerization and impingement investigation across in-air polymerization and droplet-substrate interaction.

the maximum spreading diameter, which remains comparable to that of Newtonian droplets across a range of polymer concentrations and molecular weights (Bergeron et al., 2000; Smith and Bertola, 2010; Huh et al., 2015). Nevertheless, polymer additives have been shown to influence energy dissipation mechanisms, particularly on superhydrophobic surfaces and recovery of polymer chain elasticity during impact (Chen et al., 2018). To observe the spreading and contraction behavior of viscoelastic droplet, Fang et al. (2006) employed the Oldroyd-B model for a droplet impacting a rigid plate using smoothed particle hydrodynamics. The results proved that viscoelasticity enhances the droplet spread as well as its contraction. To observe the droplet impact and spreading on an inclined plane, Jiang et al. (2010) observed that viscoelastic droplets based on the Oldroyd-B model spread faster than the Newtonian fluid. Also, for a ridged plate, Oldroyd-B-based viscoelastic models show enhanced spreading and contraction in comparison to Newtonian fluids (Tomé et al., 2002).

In the present work, we aim to simulate the key features of droplet-based microfluidic 3D printing in the case of in-air photopolymerization of micro-scale droplets ejected from a microfluidic chip and exposed to UV irradiation prior to substrate impact (**Figure 1a**). We resolve dose gradients via Beer–Lambert attenuation and kinetics to predict conversion fields prior to deposition. The coupled study of in-air photopolymerization of droplets and resulting cure-induced viscoelastic response highlights the importance of cure-induced change in viscoelastic behaviors on the droplet spreading and recoil dynamics upon impact with a surface. As photopolymerization progressively stiffens the shell through cross-linking and cure dependent viscoelastic properties. This stiffenning of the shell controls the droplet spread and recoil upon hitting a solid substrate. Therefore, controlling photopolymerization parameters directly affects the inter-droplet bonding, geometric fidelity, and layer-to-layer adhesion (**Figure 1b**). More broadly, such

control is critical for functional photopolymerized microdevices, where performance is highly sensitive to geometry and material distribution (Moughames et al., 2025). Inappropriate spreading and recoil can lead to void formation and weak interface that compromises the structural integrity and mechanical reliability of printed parts. As illustrated in **Figure 1c**, droplets experience UV irradiation during flight, leading to partial curing before deposition. Depending on the UV intensity and exposure time, we hypothesize the formation of a core-shell structure, where an uncured liquid resin core is surrounded by a partially or fully cured outer shell. For the impact modeling, the cured shell is treated as a viscoelastic material, whose mechanical response evolves with the degree of cure. Viscoelastic behavior is characterized through a cure-dependent shear modulus and relaxation time, reflecting the progressive increase in material stiffness and elastic response induced by photopolymerization. Unlike previous studies that employ single mode Oldroyd-B or Giesekus models with fixed material parameters (Faroughi et al., 2020; Mousavi and Faroughi, 2025), the present work describes the viscoelastic behavior of the material using a multi-mode relaxation spectrum composed of 10 upper-convected Maxwell elements, combined with a neo-Hookean elastic network to account for the non-relaxing response. This elastic network is triggered above the polymer gel point. The proposed framework couples the curing kinetics with impact dynamics, allowing for a physically consistent description of droplet-substrate interaction under simultaneous polymerization and deformation.

The paper is structured as follows: the first part presents the mathematical modeling of the photopolymerization process during in-air droplet flight, while the second part focuses on the incorporation of cure-induced viscoelasticity into the droplet impact model. To describe the evolution of the viscoelastic properties during curing, a multi-branch finite deformation viscoelastic constitutive model implementing multiple relaxation times is used, accounting for the cure-dependent rheological response of the droplet shell during curing and subsequent substrate interaction. The simulation of droplet impingement on the surface is based on the energy budget framework, that tracks the partitioning of kinetic energy into the elastic, dissipative, and surface energy through the impact and relaxation phases, therefore providing a mechanistic understanding of the energy pathways that govern the final shape of the printed droplet.

2 Theoretical framework

2.1 Droplet photopolymerization

The computational framework assumes a two-dimensional, incompressible, multiphase flow. Gravitational effects are neglected during the polymerization stage due to the small droplet size and short flight time. A two-phase Eulerian formulation is adopted, with air treated as the primary phase and the UV-curable resin as the secondary phase. Eulerian formulation provides each phase with a set of its own equations, therefore enabling each phase to co-exist with each other. Equation (1) is the continuity equation which enforces the mass conservation of the droplet phase through the transport of volume fraction (χ_d). Equation (2) is the momentum equation that balances the inertial forces against the pressure, viscous forces, and the interfacial surface tension force ($\mathbf{F}$). Both of these equations are implemented for a droplet as given below:

$$\frac{\partial \chi_d}{\partial t} + \nabla \cdot (\chi_d \, \mathbf{u}_d) = 0, \tag{1}$$

$$\frac{\partial (\chi_d \rho_d \mathbf{u}_d)}{\partial t} + \nabla \cdot (\chi_d \rho_d \mathbf{u}_d \mathbf{u}_d) = -\chi_d \nabla p + \nabla \cdot \left[\chi_d \eta_d \left(\nabla \mathbf{u}_d + (\nabla \mathbf{u}_d)^T \right) \right] + \mathbf{F}. \tag{2}$$

In the Eulerian framework, the pressure p is shared between both phases. Here, $\mathbf{u}_d$, ρ_d, and η_d denote the velocity, density, and viscosity of the droplet phase, respectively, and are weighted by the droplet volume fraction χ_d. The phase volume fractions satisfy

$$\chi_a + \chi_d = 1, \tag{3}$$

where χ_a denotes the volume fraction of air. The interfacial surface tension force $\mathbf{F}$ in Equation (2) is modeled using the Continuum Surface Force (CSF) formulation proposed by Brackbill et al. (1992), expressed as

$$\mathbf{F} = \sigma_{a,d} \, \kappa \, \nabla \chi_d, \tag{4}$$

where $\sigma_{a,d}$ is the surface tension coefficient between air and resin droplet, and κ is the interface curvature. The droplet density evolves during polymerization according to the degree of cure α (Tang et al., 2004):

$$\rho_d = (1 - \alpha)\rho_m + \alpha \rho_p, \tag{5}$$

where ρ_m and ρ_p represent the densities of the monomer (uncured resin) and polymer, respectively. The degree of cure α is expressed as

$$\alpha = 1 - \frac{c_m}{c_{m_0}}, \tag{6}$$

with c_{m_0} and c_m denoting the initial and instantaneous monomer concentrations. During UV exposure, the temperature field within the droplet is governed by the energy equation

$$\chi_d \rho_d C_p \left(\frac{\partial T_d}{\partial t} + \mathbf{u}_d \cdot \nabla T_d \right) = \nabla \cdot (\chi_d k_d \nabla T_d) + Q - \Delta H_r \frac{\partial c_m}{\partial t}, \tag{7}$$

where C_p, T_d, and k_d are the specific heat capacity, temperature, and thermal conductivity of the droplet, respectively. The reaction enthalpy ΔH_r is negative, indicating an exothermic polymerization process. The radiative heat source term is defined as

$$Q = IA, \tag{8}$$

where the local light intensity I follows the Beer-Lambert's law:

$$I = I_s \exp\left(- \int A(z)\, dz \right), \tag{9}$$

where z denotes the depth within the droplet and I_s is the incident light intensity. The cure-dependent absorption coefficient A, adapted from Montgomery et al. (2022), is given as

$$A = \varepsilon_i c_i + \alpha A_{poly} + (1 - \alpha) A_m, \tag{10}$$

where ε_i is the molar absorptivity of the photoinitiator, c_i is its instantaneous concentration, and A_p, A_m are the absorption coefficients of polymer and monomer, respectively. Photopolymerization proceeds through initiation, propagation, and termination reactions (Yoshida et al., 2014; Dendukuri et al., 2008). Here, we chose to model photocuring using the simplified radical photopolymerization scheme due to its relative simplicity. In radical-photopolymerization, photoinitiator molecules (In) absorb UV radiation and decompose into free radicals:

$$\mathrm{In} \xrightarrow{h\nu} 2R^* \tag{11}$$

Free radicals react with monomers to initiate polymer chains:

$$R^* + M \rightarrow RM^* \tag{12}$$

Chain propagation occurs via successive monomer addition:

$$RM^* + M \rightarrow RM_n^* \tag{13}$$

Termination occurs through radical recombination leading to dead polymer chains:

$$RM_n^* + RM_m^* \rightarrow RM_{m+n}R \tag{14}$$

In this study, three species are tracked: photoinitiator, monomer, and polymer. The initiator transport equation is modeled as a first-order reaction (Sivasankar et al., 2020; Long et al., 2009):

$$\frac{\partial (\chi_d \rho_d c_i)}{\partial t} = \nabla \cdot (\chi_d D_I \nabla c_i) - \chi_d (I_{\text{moles}} A), \tag{15}$$

where D_I is the diffusion coefficient of the photoinitiator and $I_{\text{moles}} = 4.57 \times 10^{-6} I$ (mol J^{-1}). I_{moles} is the photo flux expressed in molar units. It serves the purpose of converting radiometric intensity I(W m^{-2}) into moles of photon per unit area and per unit time. Similarly, the monomer transport equation is written as (Odian, 2004; Goodner and Bowman, 2002):

$$\frac{\partial (\chi_d \rho_d c_m)}{\partial t} = \nabla \cdot (\chi_d D_m \nabla c_m) - k_p c_m \left(\frac{\phi\, I_{\text{moles}} A}{k_t} \right)^{1/2}, \tag{16}$$

where D_m is the monomer diffusivity, ϕ is the quantum yield (number of chains initiated per photon absorbed), and k_p, k_t are the propagation and termination rate constants, respectively, which follow Arrhenius kinetics:

$$k_j = A_j \exp\left(-\frac{E_j}{RT} \right), \tag{17}$$

where A_j and E_j denote the frequency factor and molar activation energy of reaction j, respectively, with $j = p$ for propagation and $j = t$ for termination. Here, T is the absolute temperature, and R is the universal gas constant.

The current photopolymerization model provides a first-level description of the curing process. As such, it does not capture all the nonlinearities associated with free radical polymerization. The reaction rates are of Arrhenius type and do not account for diffusion-controlled kinetics. In realistic scenarios, the increase in the degree of cure reduces the mobility of species involved (initiator, monomer, and radicals). This leads to several phenomena that are not captured by the current model, such as the autoacceleration effect (also known as the Trommsdorff effect) and diffusion-limited termination at high degrees of cure (Cook, 1992). Moreover, the model overestimates species diffusivity by assuming constant diffusion coefficients of species throughout the conversion, thereby neglecting reduced chain mobility and vitrification. As a result, the curing profile predicted from the Beer-Lambert attenuation is artificially smoothed.

2.2 Cure-induced viscoelasticity

The photocuring of droplets modulates the crosslinking of monomer by considering parameters such as light intensity, exposure duration, and concentration of reactants. Tuning of any such parameter results in a strong effect on mechanical characteristics like viscoelastic effects that govern the droplet-substrate and droplet-droplet interactions. To capture cure-induced viscoelastic effects during droplet-substrate interaction, a core-shell droplet morphology is assumed (Figure 1c). The inner core consists of uncured resin, while the outer shell corresponds to the cured polymer and exhibits viscoelastic behavior. As photopolymerization progresses and the material crosses the gel point, it undergoes a transition from a purely viscous liquid to a viscoelastic solid capable of sustaining long-term mechanical loads. The gel point therefore delineates two distinct regimes in the material evolution: an equilibrium regime and a non-equilibrium regime. Following commonly adopted assumptions in the modeling of curing polymers (Wu et al., 2018), the material behavior prior to gelation is modeled as viscous melt. In this regime, the material is unable to support long-term stress and responds predominantly in a viscous manner, with only transient elastic effects. After gelation, continued polymer chain growth and crosslinking lead to a progressive increase in material stiffness, therefore enabling the material to exhibit both equilibrium (elastic) and non-equilibrium (viscoelastic) responses. In the present model, the equilibrium response is represented by a single spring, while the non-equilibrium response is modeled using a generalized Maxwell formulation, as illustrated in Figure 1c. For computational efficiency while retaining sufficient fidelity in capturing the relaxation spectrum, the non-equilibrium behavior is approximated using 10 Maxwell elements, whereas a single element is employed to represent the equilibrium elastic contribution.

The cured shell is modeled using a separate volume of fluid (VOF) equation with an additional polymeric stress term incorporated into the momentum equation:

$$\frac{\partial(\chi_d \rho_d \mathbf{u}_d)}{\partial t} + \nabla \cdot (\chi_d \rho_d \mathbf{u}_d \mathbf{u}_d) = -\chi_d \nabla p + \nabla \cdot \left[\chi_d \eta_d \left(\nabla \mathbf{u}_d + (\nabla \mathbf{u}_d)^T\right)\right] + \mathbf{F} + \nabla \cdot \boldsymbol{\tau} \tag{18}$$

where $\boldsymbol{\tau}$ is the extra polymeric stress tensor that represents the viscoelastic stress contribution for the cured shell. It is decomposed into equilibrium and non-equilibrium parts (Long et al., 2010):

$$\boldsymbol{\tau} = \boldsymbol{\tau}_{eq} + \sum_{n=1}^{10} \boldsymbol{\tau}_n \tag{19}$$

Each non-equilibrium branch is modeled using the Upper-Convected Maxwell model:

$$\overset{\triangledown}{\boldsymbol{\tau}}_n = 2\mu_n \mathbf{D} - \frac{1}{\lambda_n} \boldsymbol{\tau}_n, \tag{20}$$

where $\mathbf{D} = \frac{1}{2}\left(\nabla \mathbf{u} + (\nabla \mathbf{u})^T\right)$ is the rate of deformation tensor. Here, μ_n is the shear modulus and λ_n is the relaxation time of the n-th Maxwell element. The upper-convected derivative can also be employed for viscoelastic flows at finite deformation rates:

$$\overset{\triangledown}{\boldsymbol{\tau}}_n = \frac{\partial \boldsymbol{\tau}_n}{\partial t} + \mathbf{u} \cdot \nabla \boldsymbol{\tau}_n - (\nabla \mathbf{u}) \boldsymbol{\tau}_n - \boldsymbol{\tau}_n (\nabla \mathbf{u})^T. \tag{21}$$

The shear modulus and relaxation time are given by Losi and Knauss (1992) as:

$$\mu_n = \frac{E_n}{3}, \tag{22}$$

where E_n is the elastic modulus of the n-th Maxwell branch provided in Table A.1

$$\lambda_n = a(\alpha, T)\, \lambda_n(\alpha_{ref}, T_{g,ref}) \exp\left(-\frac{\Delta G}{k_B T} \frac{\bar{s}_n}{s_n}\right), \tag{23}$$

where $a(\alpha, T)$ is the cure- and temperature-dependent shift factor, and $\lambda_n(\alpha_{ref}, T_{g,ref})$ denotes the relaxation time at reference glass transition temperature $T_{g,ref}$. k_B is the Boltzmann constant, s_n is the athermal shear strength, while $\bar{s}_n$ is a scalar measure deviatoric stress associated with the n-th Maxwell branch. ΔG is the cure-dependent energy activation governing stress-assisted molecular relaxation. The shift factor is also given by the Williams-Landel-Ferry equation:

$$\log_{10} a(\alpha, T) = -\frac{C_1 \left[T - T_g(\alpha)\right]}{C_2 + \left[T - T_g(\alpha)\right]}, \tag{24}$$

where C_1 and C_2 are two fitting parameters provided in Table A.1. The athermal shear strength can be represented as (Boyce et al., 1988):

$$s_n = \frac{0.077\, \mu_n}{1 - \nu}, \tag{25}$$

where ν is the Poisson's ratio provided in Table A.1. The shift factor is also dependent on cure-dependent glass transition temperature (Gan et al., 1991):

$$T_g(\alpha) = \frac{E_r}{R \ln\left(g_1(1-\alpha)^{\xi} + g_2\right)}, \tag{26}$$

where E_r denotes the transition of activation energy from a glassy to rubbery state; g_1, g_2, and ξ are the material constants provided in Table A.1. The cure-dependent activation energy is given by Porter et al. (1968) as

$$\Delta G = \Delta G_0 + h \sinh\left(\frac{\alpha}{\alpha_0}\right), \tag{27}$$

where ΔG_0 is the activation energy at low degree of cure, α_0 is the critical degree of cure, and h is the empirical material constant. For the equilibrium phase, the equilibrium modulus is related to the degree of cure and gel point as (Zarrelli et al., 2010; Zhao et al., 2017):

$$E_{eq} = E_c \exp\left(b(\alpha - \alpha_{gel})\right) + E_d \tag{28}$$

where α_{gel} is the degree of cure at gel point; E_c, E_d, and b are fitting parameters. For the implementation of stress-dependent relaxation time in a two-dimensional framework (see Equation 23), we introduced a scalar measure of local deviatoric stress for each Maxwell branch $\bar{s}_n$. The objective of this scalar function is to incorporate the shear part of stress in the relaxation time using the second invariant of deviatoric stress

$$J_{2,n} = \frac{1}{2}\left[(\tau_{n,xx}^{dev})^2 + (\tau_{n,yy}^{dev})^2 + 2(\tau_{n,xy}^{dev})^2\right]. \tag{29}$$

The scalar equivalent of deviatoric stress in the n-th branch can be expressed as:

$$\bar{s}_n = \sqrt{J_{2,n}}. \tag{30}$$

The equilibrium stress part is computed as:

$$\boldsymbol{\tau}_{eq} = f(\alpha)\, \mu_{eq}\, \hat{\mathbf{B}}_{eq}, \tag{31}$$

where $\hat{\mathbf{B}}_{eq} = \frac{\mathrm{tr}(\mathbf{B}_{eq})}{3}\mathbf{I}$ is the deviatoric part, $\mu_{eq} = \frac{E_{eq}(1)}{3}$ is the fully-cured shear modulus, and $f(\alpha) = \frac{E_{eq}(\alpha)}{E_{eq}(1)}$ represents the crosslink fraction that scales the network contribution with the degree of cure. The equilibrium Cauchy stress is derived from the left Cauchy-Green deformation tensor as:

$$\mathbf{B}_{eq} = \mathbf{F}\mathbf{F}^T, \tag{32}$$

$\mathbf{B}_{eq}$ is transported using the following upper-convected kinematic relation

$$\frac{\partial \mathbf{B}_{eq}}{\partial t} + \mathbf{u} \cdot \nabla \mathbf{B}_{eq} = \mathbf{L} \cdot \mathbf{B}_{eq} + \mathbf{B}_{eq} \cdot \mathbf{L}^T, \tag{33}$$

where $\mathbf{L} = \nabla \mathbf{u}$ is the velocity gradient tensor.

3 Boundary conditions and numerical implementation

To implement the governing Equations (1)-(33), a two-dimensional computational domain of height H and width H is considered, with $H = 3D$, where $D = 100\ \mu\mathrm{m}$ denotes the initial droplet diameter. The droplet is initialized above a rigid solid substrate and impacts the surface with prescribed downward velocity of $0.7\ \mathrm{m\,s^{-1}}$ under the influence of gravity. The computational domain consists of a liquid droplet phase surrounded by air. All domain boundaries are maintained at a constant temperature of $25\ ^{\circ}\mathrm{C}$. The droplet and air phases are characterized by densities ρ_d and ρ_{air}, and dynamic viscosities η_d and η_{air}, respectively. Within the two-phase VOF framework, the local mixture properties in each computational cell are evaluated using a volume-fraction-weighted formulation (Kumar et al., 2025):

$$\eta(x,t) = \eta_{\mathrm{air}} + (\eta_{\mathrm{d}} - \eta_{\mathrm{air}})V, \tag{34}$$

$$\rho(x,t) = \rho_{\mathrm{air}} + (\rho_{\mathrm{d}} - \rho_{\mathrm{air}})V, \tag{35}$$

where V denotes the local volume fraction of the droplet phase, with $V = 0$ corresponding to pure air and $V = 1$ to pure droplet material. This formulation ensures a smooth transition of material properties across the droplet–air interface and is commonly employed in multiphase flow simulations involving sharp interfaces. The droplet is ejected from a height of $5\ \mathrm{cm}$ and encounters the UV zone of specified $(4.9\ \mathrm{mm})$. With an initial velocity from the droplet

generation system, the droplet gains additional velocity due to gravitational pull; therefore, the simulation starts with the impact velocity near the substrate. The simulation runs in two stages: (1) droplet polymerization and formation of the core-shell morphology, estimating the shell thickness and material properties of the cured shell; and (2) estimation of the spreading behavior of a cured droplet obtained from the first simulation.

For polymerization, the concentrations of reactant (monomer and photoinitiator) was set via mass fraction: photoinitiator at 0.03 and monomer at 0.97. The initial droplet temperature was ambient ($25\ ^\circ\mathrm{C}$). Gravity was disabled for the polymerization simulation. UV exposure was assumed uniform around the droplet, and the exposure duration was estimated based on the initial droplet velocity from the nozzle and height from the light source. For viscoelastic droplet impingement, a three-phase system was considered: air as the primary phase surrounding the droplet, and two secondary phases for the shell and core.

Both shell and core were modeled as Newtonian fluids with constant viscosities (ζ_s). A constant static equilibrium (θ_{eq}) was set between the shell and the substrate, defining the spreading and recoil behavior. In ANSYS Fluent software (ANSYS Inc., USA), the viscoelastic stress distribution was coupled to momentum equation through cell-level gradient reconstruction of a user-defined scalar (UDS) field. To balance computational accuracy and cost for analyzing droplet characteristics during droplet-substrate interaction, the time stepping was divided into three stages:

1. Initial impact phase (0–0.5 ms) with $\Delta t = 1 \times 10^{-8}$ s, resolving contact dynamics and avoiding stress overshoot in the stiff UDS-momentum coupling.
2. Spreading and retraction phase (0.5–5 ms) with $\Delta t = 5 \times 10^{-7}$ s.
3. Relaxation phase (5–90 ms) with $\Delta t = 5 \times 10^{-6}$ s.

4 Results and discussion

4.1 In-air photopolymerization and core–shell formation

The first part of the results examined the in-air photopolymerization of a resin droplet with diameter $D_0 = 100\ \mu\mathrm{m}$ subjected to uniform UV exposure from all sides. In practice we implemented four UV sources positioned at 90° intervals in the z-plane (Figure 1b). The narrow beam width (~ 4.9 mm) resulted in a short transit time of the droplet through the UV illumination zone. Under these conditions, gravitational acceleration was neglected and the droplet velocity v_d was assumed constant. Consequently, the exposure time is given by the kinematic relation $t_{\mathrm{exposure}} = h_{\mathrm{exposure}}/v_d$, where h_{exposure} is the vertical distance traversed within the collimated beam, corresponding to a fixed exposure duration of 7 ms for all numerical simulations. To isolate the effect of irradiation conditions, each droplet is simulated independently under a single, constant UV intensity, with four cases considered: $I_1 = 12$, $I_2 = 24$, $I_3 = 48$, and $I_4 = 96\ \mathrm{W\ cm^{-2}}$.

Figure 2a shows the spatial distribution of the degree of cure α across the droplet cross-section for the four UV intensities. The color map ranges from 0 (uncured resin) to 0.4 (maximum degree of cure reached), revealing a pronounced radial gradient in all cases. The outer region of the droplet, directly exposed to UV irradiation, attains the highest local degree of cure, while the inner core remains largely uncured. This spatial gradient arises from Beer-Lambert attenuation of the UV intensity, as described in Equations (9-10). As incident photons are absorbed by the photoinitiator, free radicals are generated, initiating polymer chain formation. The light intensity decays exponentially from the droplet surface towards its center, leading to non-uniform curing. The white lines in Figure 2a indicate the gel point (α_{gel}), which separates the mechanically coherent polymer shell ($\alpha > \alpha_{\mathrm{gel}}$) from the liquid or pre-gel interior ($\alpha < \alpha_{\mathrm{gel}}$). This interface defines the core-shell morphology for droplets polymerized under different UV intensities at the same exposure duration.

At the lowest UV intensity (I_1), the maximum degree of cure at the droplet rim is $\alpha_{1,\max} = 0.2065$, with a corresponding volume-averaged degree of cure $\alpha_{1,\mathrm{avg}} = 0.0889$. The gel-point iso-contour remains very close to the outer surface, indicating the formation of only a very thin cured shell. Under this low-irradiance condition, most of the droplet volume remains in the uncured or pre-gel state. As the UV increases from I_1 to I_4, corresponding to an 8-fold increase in intensity, α_{avg} increases by a factor of 2.31, whereas $\alpha_{\max}$ increases by a factor of 1.88. This difference indicates that the average cure state α_{avg} is more sensitive to irradiance than the local surface cure $\alpha_{\max}$, suggesting that increasing intensity promotes not only surface curing but also deeper penetration of polymerization into the droplet volume. Such graded curing is consistent with experimental observations of polyethylene glycol diacrylate (PEGDA700) droplets with inkjet technology reported by Jiang et al. (2021), where short exposure times ($1 - 5$ ms) and droplet diameters of $100 - 300\ \mu\mathrm{m}$ and limited penetration depths produced similar heterogeneous conversion profiles.

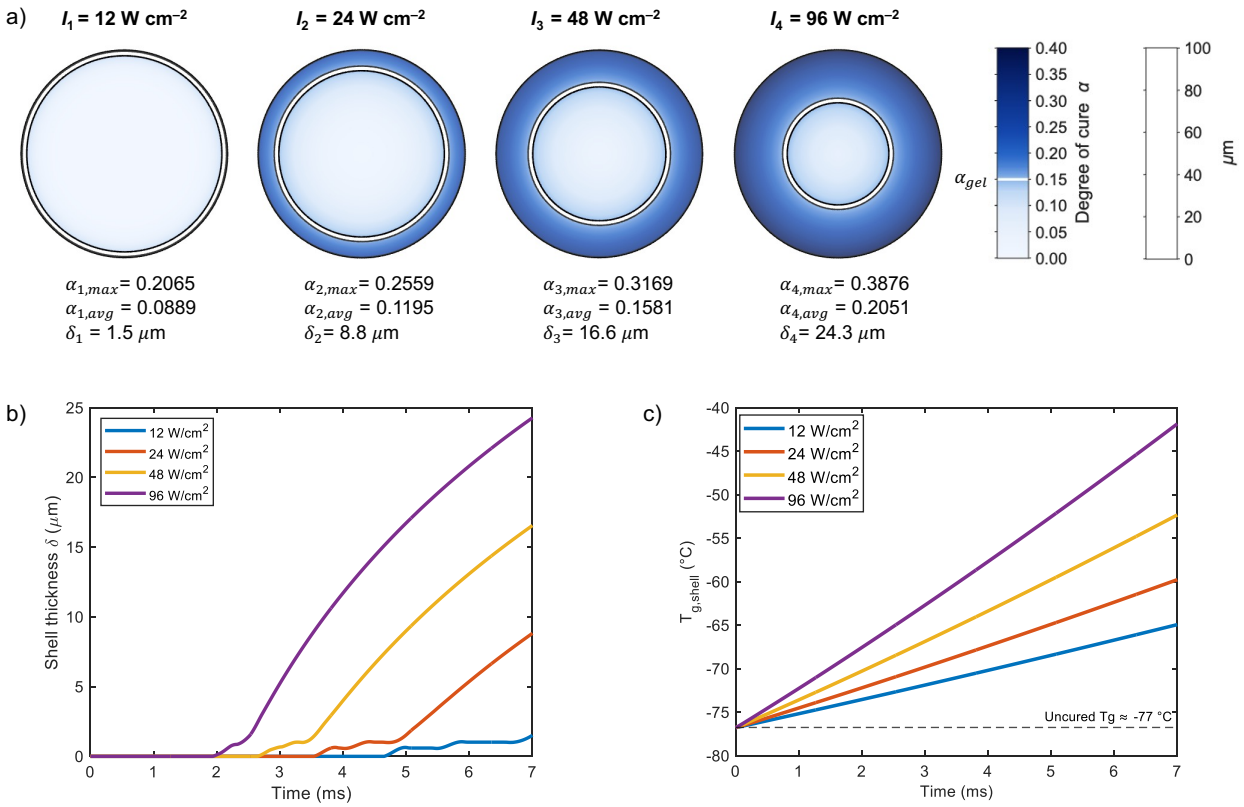

Figure 2: Cross-sectional simulation results of a UV-curable resin droplet undergoing photopolymerization from all sides in a 2D axisymmetric domain using ANSYS Fluent. (a) The degree of cure distribution is presented at increasing UV light intensities: $I_1 = 12$, $I_2 = 24$, $I_3 = 48$, and $I_4 = 96$ W cm^{-2}, after a fixed photopolymerization time of 7 ms. The color mapping represents the local degree of cure α, ranging from uncured monomer (light blue color) to cured polymer (dark blue color). The white lines indicate the approximate polymerization front, corresponding to the gel point (α_{gel}) which delineates the cured viscoelastic shell from the uncured liquid core. Droplet size $= 100$ μm. (b) Temporal evolution of shell thickness of the droplet over the four UV intensities. (c) Glass transition for a shell within 7 ms exposure over the four UV intensities.

4.2 Shell growth kinetics and glass transition evolution

The evolution of shell thickness (δ) is presented in **Figure 2b**. It is defined as the radial distance between the outer droplet surface and the gel-point iso-surface, which marks the boundary between the cured shell and the pre-gel core. Material beyond this boundary has crossed the gellation part and enterd the viscoelastic regime. A key feature is the presence of an intensity-dependent induction period, i.e., a finite delay before any measurable shell thickness appears, followed by a regime of approximately linear growth. At the lowest intensity (I_1) the induction period is ~ 5 ms, with a thin shell barely exceeding 1.5 μm. Increasing the intensity to I_4 reduces the induction period to about ~ 2 ms and promotes faster shell growth. This trend is consistent with the kinetics of photoinitiation and chain propagation. As described in Equations (11-13), the photoinitiator must first absorb a sufficient number of photons to generate radicals, after which polymer chains can propagate until the local degree reaches the gelation criterion ($\alpha = \alpha_{\text{gel}}$). At lower intensities, the rate of radical generation is slower, hence a longer time is required to reach the gel point and form a measurable shell.

The evolution of glass transition temperature over a shell (denoted $T_{g,shell}$) is presented in **Figure 2c**. This quantity is computed from the local degree of cure using Equation (26). At the onset of irradiation, all four cases exhibit the same T_g, consistent with the uncured monomer state of PEGDA250. The value of $T_{g,shell}$ increases monotonically for all irradiation cases over a period of 7 ms. The intensity I_4 yields the highest $T_{g,shell}$ of -42 °C, whereas I_1 results in the lowest value of -65 °C. The ordering with respect to intensity is preserved throughout the exposure time (7 ms), such that $T_{g,shell}\ (I_4) > T_{g,shell}\ (I_3) > T_{g,shell}\ (I_2) > T_{g,shell}\ (I_1)$. This behavior is a direct consequence of the monomer consumption rate $k_p c_m \sqrt{\frac{\phi\, I_{\text{moles}}\, A}{k_t}}$, which makes the cure rate a sublinear function of the local intensity. Consequently,

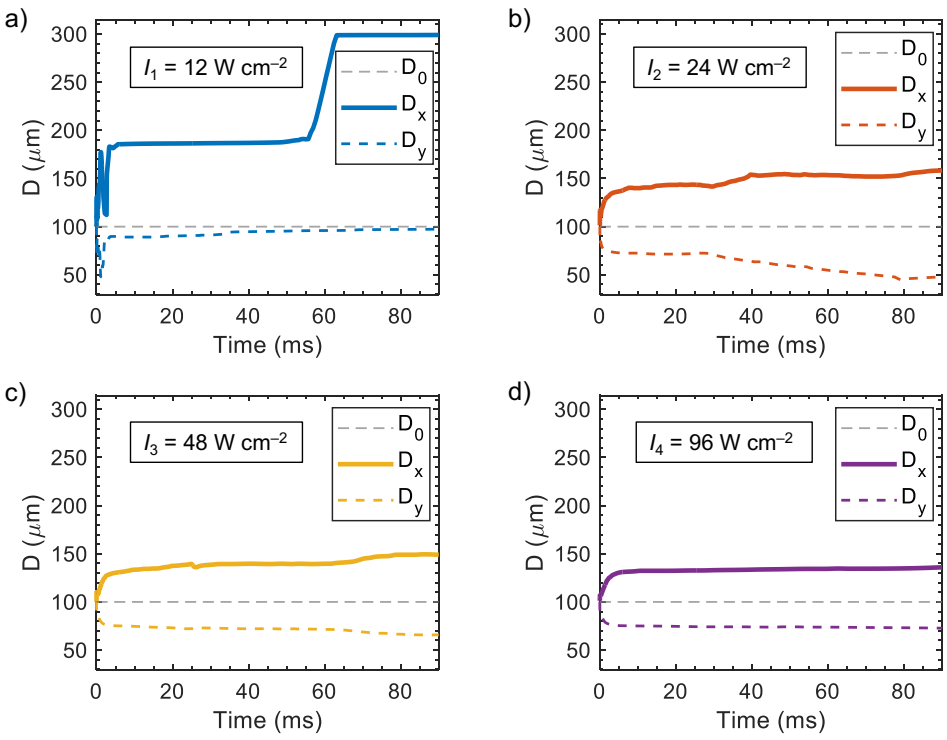

Figure 3: Spreading behavior of a 100 μm droplet with an impact velocity of 0.7 $\mathrm{m\,s^{-1}}$. Each of the four graphs corresponds to the cases presented in Figure 2a for an UV exposure of (a) $I_1 = 12\ \mathrm{W\,cm^{-2}}$, (b) $I_2 = 24\ \mathrm{W\,cm^{-2}}$, (c) $I_3 = 48\ \mathrm{W\,cm^{-2}}$, and (d) $I_4 = 96\ \mathrm{W\,cm^{-2}}$.

doubling the intensity does not lead to a doubling of T_g, and the difference between the maximum and minimum values at 7 ms is approximately 12 °C. This variation reflects the logarithmic intensity dependence of T_g on the degree of cure. Since the predicted values remain below the ambient temperature, the cured shell is expected to behave as a deformable viscoelastic material (in the rubbery regime) rather than as a glassy solid. This explains why the shell can undergo substantial deformation during spreading while storing sufficient elastic energy to contribute to recoil.

4.3 Droplet impingement

The core-shell configurations obtained under four UV intensities are used to simulate droplet impingement onto a solid substrate with an impact velocity of 0.7 $\mathrm{m\,s^{-1}}$. **Figure 3** shows the temporal evolution of the horizontal (D_x) and vertical (D_y) interface diameters for each irradiated droplet. For the highest intensity ($I_4 = 96\ \mathrm{W\,cm^{-2}}$), which produces the thickest shell, the spreading is smooth and monotonic. The droplet expands from 100 μm to 135 μm within the first 30 ms, after which the evolution reaches a plateau, with only about 2 μm of additional change over the next 60 ms. The equilibrium spreading ratios are $\beta_x \approx 1.35$ and $\beta_y \approx 0.72$. No oscillations or retractions is observed, indicating an overdamped response in which the viscoelastic shell suppresses transient overshoot (**Figure 3a**). It is worth noting that the droplet transitions directly from its spherical impact configuration to a flattened sessile state along a single irreversible path. For intensities of 48 $\mathrm{W\,cm^{-2}}$ (I_3) and 24 $\mathrm{W\,cm^{-2}}$ (I_2), corresponding to shell thickness of 16.5 μm and 9 μm, respectively, the initial spreading resembles that of the 96 $\mathrm{W\,cm^{-2}}$ (I_4) case. However, the droplet does not fully stabilize. A secondary spreading phase occurs, during which D_x slightly increases stepwise. This late-stage creep arises from the competition between the elastic network and capillary forces. While the network is strong enough to arrest the initial inertia-driven spreading, it cannot indefinitely resist sustained capillary pressure. Over time, the capillary forces exceed the elastic resistance, leading to a slow, viscous creep. This behavior represents a transitional regime between spreading and complete arrest (**Figure 3b** and **Figure 3b**). In contrast, for the thinnest shell (1.5 μm), corresponding to a UV intensity of 12 $\mathrm{W\,cm^{-2}}$ (I_1), the degree of cure of the shell is close to the gel point, and the spreading behavior differs significantly from the one of the solid shell. During the initial contact phase, the droplet exhibits oscillations, characteristic of a Newtonian liquid at low Weber number. Then, the droplet shape reaches a metastable "pancake" shape, until a sudden transition occurs at ~ 60 ms where D_x jumps from 190 to 300 μm. This may be related to a shell failure, leading to a collapse of the droplet (**Figure 3d**).

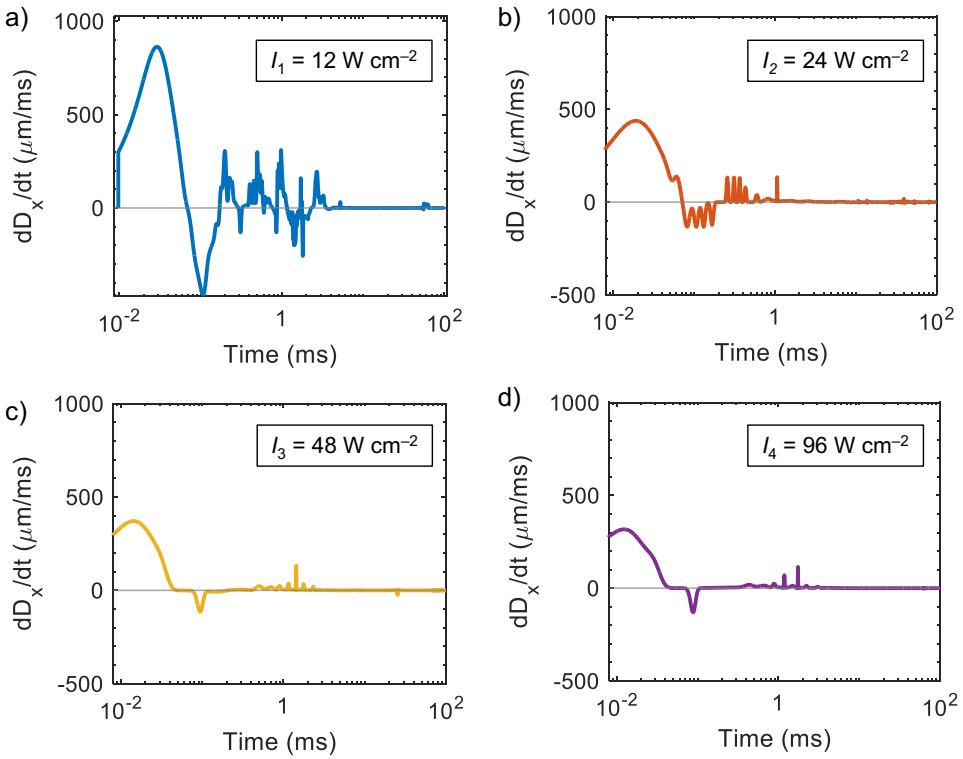

Figure 4: Radial velocity profile of the contact line between a 100 μm droplet with an impact velocity of 0.7 $\mathrm{m\,s^{-1}}$ and substrate. Each of the four graphs corresponds to the cases presented in Figure 2a for an UV exposure of (a) $I_1 = 12\ \mathrm{W\,cm^{-2}}$, (b) $I_2 = 24\ \mathrm{W\,cm^{-2}}$, (c) $I_3 = 48\ \mathrm{W\,cm^{-2}}$, and (d) $I_4 = 96\ \mathrm{W\,cm^{-2}}$.

Table 1 summarizes the morphological data extracted from the spreading behavior of each core-shell configuration. The final spreading ratio β_x increases from 1.35 to 2.99 as the intensity decreases from 96 to 12 $\mathrm{W\,cm^{-2}}$. Conversely, the vertical compression ratio β_y decreases, indicating progressive flattening of the droplet. At 12 $\mathrm{W\,cm^{-2}}$ (I_1), the droplet approaches a nearly flat disk shape. The late-time spreading rate, $\mathrm{d}\beta_x/\mathrm{d}t$ (averaged over 30–90 ms), increases from 0.03 to 1.88 as the intensity decreases from 96 to 12 $\mathrm{W\,cm^{-2}}$.

Figure 4 shows the radial velocity profile of the contact line between the droplet and the substrate. This profile illustrates shell velocity at the interface as it advances and retracts during droplet-substrate interaction for all four intensities on the logarithmic time axis. All four cases exhibit a single well defined peaks. The peak velocity increases as the intensity increases from intensities I_1 to I_4. In case of intensity I_4, the droplet experiences peak spreading velocity of 313 $\mu\mathrm{m\,s^{-1}}$, which increases to 368.488 $\mu\mathrm{m\,s^{-1}}$ and 436.529 $\mu\mathrm{m\,s^{-1}}$ for I_3 and I_2, respectively. At intensity I_4, the velocity decay experiences a single negative peak of moderate amplitude that recovers very swiftly to zero. Here, The low maximum and rapid decay indicate that the contact line of shell is arrested within a short time. Also, the small amplitude of oscillation define the system as overdamped. This means elastic energy is mostly dissipated via viscoelastic branches rather than being converted back to kinetic energy. For intensity I_3 (**Figure 4c**), the velocity profile is quite similar to intensity I_4, but shows a higher peak value. At intensity I_2 (**Figure 4b**), the droplet experiences a remarkable change. The peak is higher than that of intensities I_3 and I_4, and the decay is followed by low-frequency oscillations. This is the representation of slow creep, where the capillary forces dominate the elastic forces, therefore representing a weekly elastic or pure viscous drop. These low amplitude oscillations in the negative velocity zone associated with intensity I_2 are responsible for shell deformation. **Figure 4a** represents the complex droplet dynamics for intensity I_1, were the shell thickness and the degree of cure associated are extremely low. The spreading velocity peaks at 846.6 $\mathrm{W\,cm^{-2}}$ and shows large negative velocities that co-relate with its corresponding spreading plots (**Figure 3a**). These oscillations indicate absence of elastic shell or inefficient elastic shell that spread freely under inertial and capillary forces.

Table 1: Spreading and shape characteristics at $0.7\ \mathrm{m\,s^{-1}}$. The aspect ratio D_x/D_y is evaluated at $t = 90$ ms.

I ($\mathrm{W\,cm^{-2}}$)	δ (μm)	$\beta_{x,90}$	$\beta_{y,90}$	$D_{x,90}$ (μm)	$D_{y,90}$ (μm)	D_x/D_y	$\mathrm{d}\beta_x/\mathrm{d}t$	Characteristic
96	24.2	1.35	0.72	135	72	1.85	0.03	Arrested
48	16.5	1.50	0.65	150	65	2.30	0.17	Creep
24	9.00	1.59	0.45	159	45	3.30	0.28	Slow spread
12	1.50	2.99	≈ 1.0	299	≈ 98	≈ 3.05	1.88	Runaway

4.4 Energy budget

The spreading data discussed above describe the droplet-substrate interaction; however, the underlying mechanisms can be better understood through an energy analysis. The total energy (E_{k0}) is decomposed into kinetic (E_k), surface (E_s), elastic (E_{el}), gravitational (E_g), and dissipative (E_d) contributions, as given by Mobaseri et al. (2025):

$$E_{k0} = E_k + \Delta E_s + E_d + E_{el} + \Delta E_g. \tag{36}$$

The kinetic energy is defined as $E_k = \int \frac{1}{2}\rho v^2\, dV$, while the surface energy is given by $E_s = \int \gamma\delta\, dV$, where δ is the Brackbill CSF surface area density. The elastic energy E_{el} consists of both equilibrium and non-equilibrium parts. **Figure 5** shows the normalized kinetic energy (E_k/E_{k0}) for all four studied core-shell droplets on a logarithmic time scale. The time it takes for E_k to drop to half of its initial value ("half-life") decreases with increasing shell hardness, indicating that higher curing levels and thicker shells lead to faster energy dissipation. The decay times follow the order: $24.5\ \mu$s (I_1) $> 12.0\ \mu$s (I_2) $> 9.8\ \mu$s (I_3) $> 8.7\ \mu$s (I_4). The rapid dissipation in thicker, more cured shells can be attributed to higher effective viscosities and additional losses through non-equilibrium Maxwell branches during high-strain-rate impact. Moreover, case I_1 ($12\ \mathrm{W\,cm^{-2}}$) exhibits a secondary peak of 29.2% at $t = 0.87$ ms, which may indicate a rebound event where some energy is converted back into motion (**Figure 5d**). The suppression of oscillations in cases I_2, I_3, and I_4 is associated with the strengthening of the equilibrium elastic network above the gel point. A delay is observed in the case of the droplet with the thinner shell, for which the normalized kinetic energy remains high for larger than for the droplets having harder shells upon impact. This may indicate that the droplet with thinner shell behaves close to a plain liquid droplet, with its kinetic energy contributing for larger to deformational motion.

Further insight into spreading behavior is obtained from the normalized elastic energy (E_{el}/E_{k0}). **Figure 5b** shows the temporal evolution of the instantaneous normalized elastic energy for all configurations. For intensity I_1, where $\alpha_{\max} \approx \alpha_{gel}$, E_{el} remains negligible throughout the simulation due to the absence of a sufficiently developed permanent network. In contrast, for the remaining configurations, E_{el} increases during spreading, reaches a peak, and then decays as the system relaxes. The elastic energy storage is maximal for intermediate shell thickness (as observed for intensity I_2). The time to reach peak elastic energy shifts from 5.4 ms (I_2) to 4.1 ms (I_3) to 0.5 ms (I_4), indicating that stiffer shells attain maximum deformation more rapidly. Notably, the elastic energy does not vary monotonically with shell thickness. This behavior can be explained by the scaling relation:

$$E_{el} \sim \mu_{eq}(\alpha)\, \varepsilon^2\, V_{\text{shell}}, \tag{37}$$

where ε is the deformation strain, $\mu_{eq}(\alpha)$ is the effective shear modulus of the polymer for a given degree of cure α, and V_{shell} is the volume of the cured shell region of the droplet. For intensity I_2, the elastic network is relatively compliant ($f(\alpha) \approx 0.08$), allowing significant capillary-driven spreading ($D_x/D_0 = 1.58$ at 90 ms) and thus large deformation strains. In contrast, for UV intensity I_4, the network is stiffer ($f(\alpha) \approx 0.18$), but spreading is arrested early ($D_x/D_0 = 1.35$), limiting strain development. Consequently, the product $\mu_{eq}(\alpha)\varepsilon^2$ is maximized at an intermediate curing state, where shell is sufficiently stiff to store energy but still compliant to undergo deformation. In all case, E_{eq} goes back to zero at long times, indicating that elastic energy is temporarily stored and later released or dissipated.

This result has direct implications for droplet-based additive manufacturing, i.e., the highest recoil tendency occurs not at the highest curing level, but at an intermediate state just above the gel point. A key question arising from Figure 5b is how elastic energy, constituting only 1–4% of the initial kinetic energy, can significantly influence droplet dynamics. It is important to note that the reported elastic energy is averaged over the entire droplet, including the uncured core. In reality, elastic stresses are concentrated within the shell, particularly near the contact line where deformation gradients are highest. For example, in case of the hardest droplet (I_4) (**Figure 5c**), the effective elastic stress at the contact line can be estimated as $\sigma_{el} \approx \mu_{eq}\varepsilon \approx 15.7$ kPa, while the capillary pressure is $\gamma/R \approx 700$ Pa. Thus, the elastic stress exceeds the capillary pressure by a factor of approximately 22, which explains the strong arrest of spreading despite the relatively small global energy contribution. The dissipation mechanisms are illustrated in **Figure 5d** for I_1 ($12\ \mathrm{W\,cm^{-2}}$) and **Figure 5e** for I_4 ($96\ \mathrm{W\,cm^{-2}}$). At low intensity, viscous dissipation Φ_{visc} dominates the early impact regime, indicating liquid-like behavior where energy loss is governed by internal shear. From intensities I_2 to

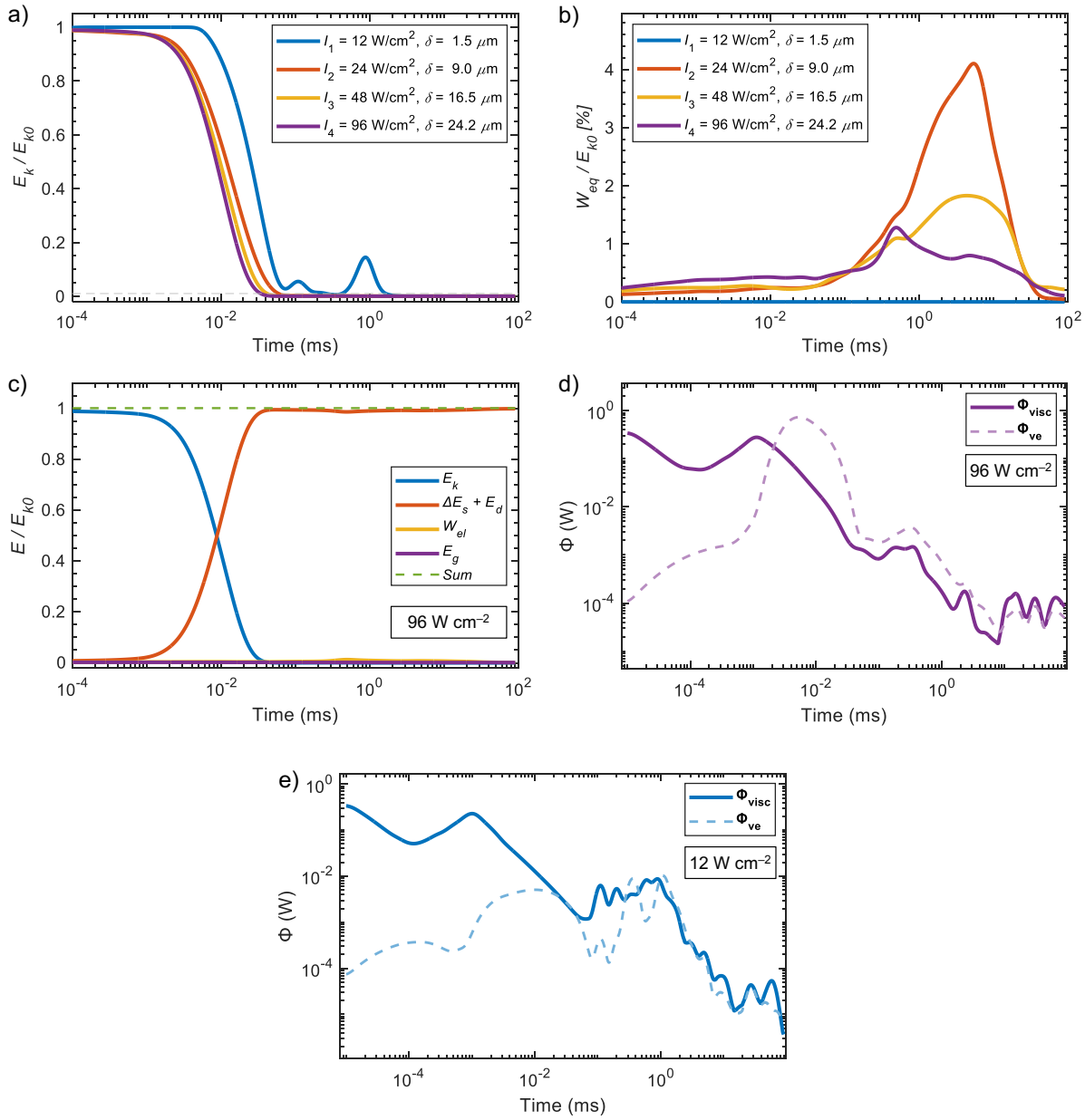

Figure 5: Computation of the droplet total energy on impact with a substrate. (a) Normalized kinetic energy for all four studied core-shell droplets on a logarithmic time axis (b) normalized equilibrium elastic energy evolution, (c), normalized mechanical energy budget for I_4 (96 W cm^{-2}), (d) dissipation rates for droplet at I_4 (96 W cm^{-2}), and (e) dissipation rates for droplet at I_1 (12 W cm^{-2}).

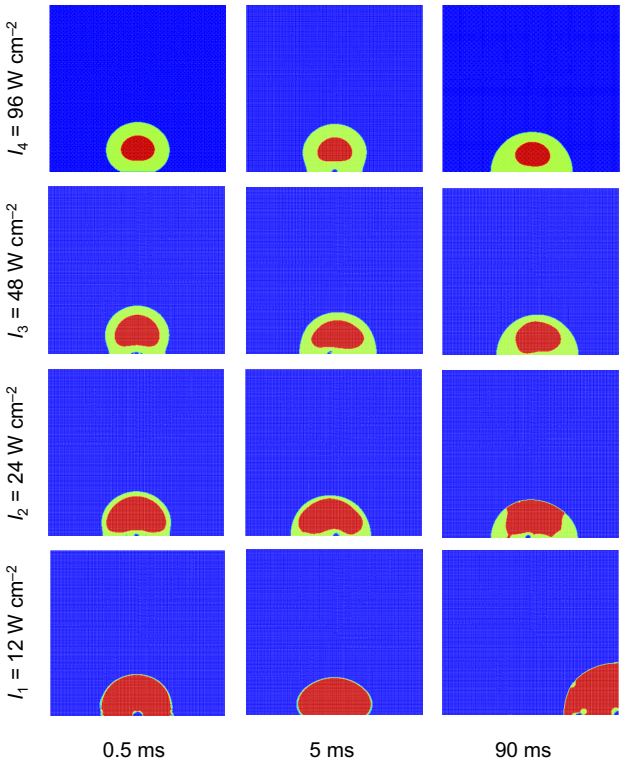

Figure 6: Spatial distribution of phase fraction for the four droplets studied. Rows correspond to specific UV intensities ($I_4 = 96\ \mathrm{W\,cm^{-2}}$, $I_3 = 48\ \mathrm{W\,cm^{-2}}$, $I_2 = 24\ \mathrm{W\,cm^{-2}}$, and $I_1 = 12\ \mathrm{W\,cm^{-2}}$), while columns represent different time steps. The colors indicate the phases type as follows: shell (green), core (red), and air (blue). For harder droplets, the core phase region remains localized and compact, whereas softer shells lead to broader and more diffuse phase distributions, indicating enhanced spreading.

I_4, viscoelastic dissipation Φ_{ve} increases rapidly and surpasses viscous dissipation during the early spreading phase ($t \sim 10^{-3}$ to 10^{-1} ms), which reflects a transition regime where both hydrodynamic and elastic effects are significant. At the highest intensity (I_4), viscoelastic dissipation dominates the early-time response, peaking between 10^{-3} and 10^{-2} ms due to stress buildup and relaxation within the crosslinked shell. For $t > 1$ ms, both dissipation mechanisms decrease and exhibit fluctuations associated with interfacial (capillary) dynamics. These results demonstrate how cure-induced rheological changes (governed by α and δ) alter the energy pathways, thereby controlling the droplet spreading dynamics.

The droplet-substrate interaction can be visualized in **Figure 6**, where the air phase is represented in blue color, the cured shell in green color, and the uncured core in red color. The images are obtained at three distinct instants 0.5 ms, 5 ms, and 90 ms. The core-shell configuration is obtained by the Beer-Lambert attenuation, therefore, at intensity I_4 ($96\ \mathrm{W\,cm^{-2}}$) the shell thickness is visible while, as for intensity I_1 ($12\ \mathrm{W\,cm^{-2}}$), this green region is barely visible. The shell maintains the almost a uniform thickness across all the three frames at intensity I_4. During the interaction with the substrate, The viscoelastic shell is under compression (at the substrate level) and tension (at the center), but still it holds, as the stress is distributed in the cross-linked shell and dissipating viscous energy through the non-equilibrium nodes. For intensity I_3 ($48\ \mathrm{W\,cm^{-2}}$) at 90 ms, we observe a thin shell at the contact line. The distribution of shell becomes drastic for intensity I_2 ($24\ \mathrm{W\,cm^{-2}}$) and we can see the core exposed from the top. It stores the highest elastic energy by virtue of its deformation that ultimately results in the shell rupture. In case of intensity I_1 ($12\ \mathrm{W\,cm^{-2}}$), the shell has lost the structural coherence, leading to exposed core, that is subjected to capillary actions, thus drifting the core from its actual position.

Conclusion

This work established a theoretical framework for predicting the behavior of in–air photopolymerized droplets, which addresses the fundamental question of how curing conditions dictate the final morphology of droplet in droplet-based

3D printing. By considering compressible two-phase flow with energy, species transport, and radiative attenuation governed by the Beer–Lambert law, the model captures the formation of heterogeneous core–shell structures during flight. A key contribution of this study is the introduction of a cure-dependent viscoelastic shell formulation based on the Olroyd-B style Maxwell model, in which the evolving mechanical response is decomposed into equilibrium (elastic) and non-equilibrium (viscous) components. By explicitly linking relaxation time and moduli to the degree of cure, the numerical framework enables a physics-based description of how material properties evolve dynamically during photopolymerization and directly influence droplet impingement behavior.

The results demonstrate that UV intensity and exposure time govern not only the thickness of the cured shell but also its mechanical dominance during substrate interaction. High-intensity irradiation promotes the formation of a sufficiently thick and stiff shell, leading to arrested spreading and an overdamped response. In this regime, elastic stresses at the contact line significantly exceed capillary forces, therefore suppressing recoil and stabilizing droplet shape. A transitional regime is identified at intermediate UV intensities, where elastic and capillary forces become comparable, which marks a shift in impact dynamics. At lower UV intensities, the shell loses mechanical integrity, which results in pronounced deformation, oscillations, and exposure of the liquid core, with spreading governed primarily by core–substrate interactions. Beyond these physical insights, the proposed framework serves as a predictive design tool for droplet-based additive manufacturing. By mapping material and process parameters, such as resin formulation, UV intensity, exposure duration, and impact velocity, to final droplet morphology, the framework enables rational selection of operating conditions to achieve controlled deposition outcomes, ranging from fully arrested droplets to tailored spreading profiles.

Looking forward, this work defines a clear pathway toward the complete realization of microfluidic droplet-based 3D printing. A critical next step is the extension of the present single-droplet framework to multi-droplet interactions, including stacking, coalescence, and interfacial bonding between partially cured droplets. These interactions ultimately determine layer integrity, geometric accuracy, and mechanical performance of printed structures. Incorporating inter-droplet diffusion, curing continuity across interfaces, and evolving viscoelastic contact mechanics will be essential to capture these effects. Equally important is experimental validation of the proposed framework through in-air photopolymerization setups combined with high-speed imaging and spectroscopic diagnostics to resolve transient curing and core–shell formation. In particular, a multi-source irradiation strategy will be implemented experimentally to approximate the uniform all-around exposure assumed in the simulations and to quantify how illumination non-uniformity affects spatial conversion gradients and core–shell development during in-flight curing. Such validation will not only confirm model predictions but also inform parameter calibration and material-specific constitutive behavior.

Declaration of competing interest

The authors declare that they have no known competing financial interests or personal relationships that could have appeared to influence the work reported in this paper.

Data availability

Data will be made available on request.

Acknowledgments

This work was supported by the French National Research Agency (ANR) under grant number ANR-23-CE10-0018-01 (“VOXWRITE”). The authors gratefully acknowledge the Mésocentre de Calcul at Université Marie et Louis Pasteur, where the development and simulations presented in this work were performed.

A Simulation parameters

Table A.1: Material properties and model parameters.

Parameter	Definition	Value	Reference
ρ_m	Density of Monomer	$1100\ \mathrm{kg\,m^{-3}}$	
ρ_p	Density of polymer	$1222\ \mathrm{kg\,m^{-3}}$	
u_d	Velocity of droplet	$0.7\ \mathrm{m\,s^{-1}}$	
$\sigma_{(a,d)}$	Surface tension (shell–air)	$0.035\ \mathrm{N\,m^{-1}}$	
θ_{eq}	Equilibrium contact angle	90°	
ε_i	Molar absorptivity (photoinitiator)	$150\ \mathrm{m^2\,mol^{-1}}$	Odian (2004)
A_p	Absorption coefficient (polymer)	$1.81 \times 10^3\ \mathrm{m^{-1}}$	Wu et al. (2018)
A_m	Absorption coefficient (monomer)	$0\ \mathrm{m^{-1}}$	Wu et al. (2018)
D_I	Diffusion coefficient (initiator)	$1.0 \times 10^{-10}\ \mathrm{m^2\,s^{-1}}$	Fang et al. (2004)
D_m	Diffusion coefficient (monomer)	$1.0 \times 10^{-10}\ \mathrm{m^2\,s^{-1}}$	Fang et al. (2004)
ϕ	Quantum yield	0.6	Goodner and Bowman (2002)
A_p	Frequency factor (propagation)	$5 \times 10^{10}\ \mathrm{L\,mol^{-1}\,s^{-1}}$	Sivasankar et al. (2020)
A_t	Frequency factor (termination)	$1.2 \times 10^{12}\ \mathrm{L\,mol^{-1}\,s^{-1}}$	Sivasankar et al. (2020)
E_p	Activation energy (propagation)	$29.7\ \mathrm{kJ\,mol^{-1}}$	Sivasankar et al. (2020)
E_t	Activation energy (termination)	$22.2\ \mathrm{kJ\,mol^{-1}}$	Sivasankar et al. (2020)
T_d	Initial droplet temperature	$25\ ^\circ\mathrm{C}$	
R	Universal gas constant	$8.314\ \mathrm{J\,mol^{-1}\,K^{-1}}$	
C_p	Specific heat capacity of droplet	$4185\ \mathrm{J\,kg^{-1}\,K^{-1}}$	Minea (2021)
k_d	Thermal conductivity of droplet	$0.3\ \mathrm{W\,m^{-1}\,K^{-1}}$	Kasper (2022)
ΔH_r	Heat of polymerization	$-50\ \mathrm{kJ\,mol^{-1}}$	Goodner and Bowman (2002)
η_d	Droplet viscosity	$0.01\ \mathrm{Pa\,s}$	Webber et al. (2024)
E_n	Young's modulus (10 branches)	$3.19, 5.69, 10.56, 19.44, 27.71,$ $42.54, 47.10, 59.3, 57.60, 64.19\ \mathrm{MPa}$	Wu et al. (2018)
λ_n	Relaxation times (10 nodes)	$6.07, 671.7, 10.18, 0.157,$ $3.27 \times 10^{-3}, 5.64 \times 10^{-5},$ $7.25 \times 10^{-7}, 6.88 \times 10^{-9},$ $5.63 \times 10^{-11}, 3.09 \times 10^{-13}\ \mathrm{s}$	Wu et al. (2018)
C_1, C_2	WLF parameters	$6.1 \times 10^4,\ 511.792\ ^\circ\mathrm{C}$	Wu et al. (2018)
ν	Poisson's ratio	0.499	Wu et al. (2018)
E_r	Transition activation energy	$18959\ \mathrm{J\,mol^{-1}}$	Wu et al. (2018)
g_1, g_2, ξ	Material constants	$109603,\ 722.20,\ \xi$	Wu et al. (2018)
ΔG_0	Activation energy (low cure)	$0\ \mathrm{J}$	Wu et al. (2018)
α_0	Critical degree of cure	0.0683	Wu et al. (2018)
α_{gel}	Gel point conversion	0.20	
E_c, E_d, b	Fitting parameters	$1.059,\ 3.321,\ 5.248\ \mathrm{MPa}$	Wu et al. (2018)
h	Empirical constant	$6.858 \times 10^{-25}\ \mathrm{J}$	Wu et al. (2018)

References

Alves, M., Oliveira, P., Pinho, F., 2021. Numerical methods for viscoelastic flows. Annual Review of Fluid Mechanics 53, 509–541. doi:10.1146/annurev-fluid-010719-060146.

Bartolo, D., Boudaoud, A., Narcy, G., Bonn, D., 2007. Dynamics of non-newtonian droplets. Physical Review Letters 99, 174502. doi:10.1103/PhysRevLett.99.174502.

Bera, A., Sivasankar, V., Das, S., 2025. Coalescence and mixing of a polymeric drop impacting on a dissimilar, miscible polymeric liquid film. Physics of Fluids 37. doi:10.1063/5.0270238.

Bergeron, V., Bonn, D., Martin, J., Vovelle, L., 2000. Controlling droplet deposition with polymer additives. Nature 405, 772–775. doi:10.1038/35015532.

Bird, R., Armstrong, R., Hassager, O., 1986. Dynamics of Polymeric Liquids. Wiley.

Bouillant, A., Dekker, P.J., Hack, M.A., Snoeijer, J.H., 2022. Rapid viscoelastic spreading. Phys. Rev. Fluids 7, 123604. doi:10.1103/PhysRevFluids.7.123604.

Boyce, M., Parks, D., Argon, A., 1988. Large inelastic deformation of glassy polymers. Part I: rate dependent constitutive model. Mechanics of Materials 7, 15–33. doi:10.1016/0167-6636(88)90003-0.

Brackbill, J., Kothe, D., Zemach, C., 1992. A continuum method for modeling surface tension. Journal of Computational Physics 100, 335–354. doi:10.1016/0021-9991(92)90240-Y.

Chakrabarti, A., Porat, A., Raphaël, E., Salez, T., Chaudhury, M.K., 2018. Elastowetting of soft hydrogel spheres. Langmuir 34, 3894–3900. doi:10.1021/acs.langmuir.8b00368. pMID: 29533669.

Chen, L., Wang, Y., Peng, X., Zhu, Q., Zhang, K., 2018. Impact dynamics of aqueous polymer droplets on superhydrophobic surfaces. Macromolecules 51, 7817–7827. doi:10.1021/acs.macromol.8b01310.

Cohen, N., Foster, R., Mow, V., 1998. Composition and dynamics of articular cartilage: structure, function, and maintaining healthy state. Journal of Orthopaedic & Sports Physical Therapy 28, 203–215. doi:10.2519/jospt.1998.28.4.203.

Cook, W.D., 1992. Thermal aspects of the kinetics of dimethacrylate photopolymerization. Polymer 33, 2152–2161.

De Ruiter, R., Royon, L., Snoeijer, J., Brunet, P., 2018. Drop spreading and gelation of thermoresponsive polymers. Soft Matter 14, 3096–3104. doi:10.1039/C8SM00047K.

Dendukuri, D., Panda, P., Haghgooie, R., Kim, J., Hatton, T., Doyle, P., 2008. Modeling of oxygen-inhibited free radical photopolymerization in a PDMS microfluidic device. Macromolecules 41, 8547–8556. doi:10.1021/ma8017717.

Fang, J., Owens, R., Tacher, L., Parriaux, A., 2006. A numerical study of the SPH method for simulating transient viscoelastic free surface flows. Journal of Non-Newtonian Fluid Mechanics 139, 68–84. doi:10.1016/j.jnnfm.2006.07.002.

Fang, N., Sun, C., Zhang, X., 2004. Diffusion-limited photopolymerization in scanning micro-stereolithography. Applied Physics A 79, 1839–1842.

Faroughi, S., Fernandes, C., Nóbrega, J., McKinley, G., 2020. A closure model for the drag coefficient of a sphere translating in a viscoelastic fluid. Journal of Non-Newtonian Fluid Mechanics 277, 104218. doi:10.1016/j.jnnfm.2019.104218.

Feng, Y., Liu, J., Deng, J., Zhang, S., Liu, Y., 2024. A review on droplet-based 3d printing with piezoelectric micro-jet device. Smart Materials and Structures 33, 073003.

Gan, S., Seferis, J., Prime, R., 1991. A viscoelastic description of the glass transition-conversion relationship for reactive polymers. Journal of Thermal Analysis and Calorimetry 37, 463–478. doi:10.1007/BF01913098.

Gilani, N., Foerster, A., Aboulkhair, N.T., 2023. Material jetting, in: Springer Handbook of Additive Manufacturing. Springer, pp. 371–387.

Goodner, M., Bowman, C., 2002. Development of a comprehensive free radical photopolymerization model incorporating heat and mass transfer effects in thick films. Chemical Engineering Science 57, 887–900. doi:10.1016/S0009-2509(01)00389-0.

Hu, S., Zhu, W., Yang, W., Li, M., 2022. Morphology simulation of drop-on-demand inkjet-printed droplets. npj Flexible Electronics 6, 64.

Huh, H., Jung, S., Seo, K., Lee, S., 2015. Role of polymer concentration and molecular weight on the rebounding behaviors of polymer solution droplet impacting on hydrophobic surfaces. Microfluidics and Nanofluidics 18, 1221–1232. doi:10.1007/s10404-014-1518-4.

Im, B., Prasetyo, F.D., Yudistira, H.T., Khalil, S.M., Cho, D.H., Byun, D., 2023. Drop-on-demand electrohydrodynamic jet printing of microlens array on flexible substrates. ACS Applied Polymer Materials 5, 2264–2271.

Jiang, J., Shea, G., Rastogi, P., Kamperman, T., Venner, C.H., Visser, C.W., 2021. Continuous high-throughput fabrication of architected micromaterials via in-air photopolymerization. Advanced materials 33, 2006336.

Jiang, T., Ouyang, J., Yang, B., Ren, J., 2010. The SPH method for simulating a viscoelastic drop impact and spreading on an inclined plate. Computational Mechanics 45, 573–583. doi:10.1007/s00466-009-0430-2.

Karakaya, E., Bider, F., Frank, A., Teßmar, J., Schöbel, L., Forster, L., Schrüfer, S., Schmidt, H.W., Schubert, D.W., Blaeser, A., et al., 2022. Targeted printing of cells: Evaluation of ada-peg bioinks for drop on demand approaches. Gels 8, 206.

Kasper, P.C., 2022. Demonstration of a Transient Hot Wire Measurement System Towards a Carbide-Based Sensor for Measuring the Thermal Conductivity of Molten Salts. Master's thesis. Brigham Young University.

Khalil, S.M., Ali, S., Nguyen, V.D., Cho, D.H., Byun, D., 2025. High-precision drop-on-demand printing of charged droplets on nonplanar surfaces with machine learning. Advanced Intelligent Systems 7, 2400621.

Kim, A.R., Mitra, S., Shyam, S., Zhao, B., Mitra, S.K., 2024. Flexible hydrogels connecting adhesion and wetting. Soft Matter 20, 5516–5526. doi:10.1039/D4SM00022F.

Kumar, R., Pal, G., Sharma, C., 2025. Pinning mediated coalescence-induced lateral droplet motion on nanotextured superhydrophobic surface. doi:10.48550/arXiv.2507.22547, arXiv:2507.22547.

Layani, M., Wang, X., Magdassi, S., 2018. Novel materials for 3d printing by photopolymerization. Advanced Materials 30, 1706344. doi:10.1002/adma.201706344.

Lee, J.H., Jang, T., Park, S., Shin, S.B., Lee, J., Hwang, Y.H., Lee, H., 2026. 3d printing of droplet microfluidic devices: Principles, wetting control, scale-up, and beyond. Lab on a Chip .

Ligon, S., Liska, R., Stampfl, J., Gurr, M., Mülhaupt, R., 2017. Polymers for 3d printing and customized additive manufacturing. Chemical Reviews 117, 10212–10290. doi:10.1021/acs.chemrev.7b00074.

Long, K., Dunn, M., Qi, H., 2010. Mechanics of soft active materials with phase evolution. International Journal of Plasticity 26, 603–616. doi:10.1016/j.ijplas.2009.10.003.

Long, K., Scott, T., Qi, H., Bowman, C., Dunn, M., 2009. Photomechanics of light-activated polymers. Journal of the Mechanics and Physics of Solids 57, 1103–1121. doi:10.1016/j.jmps.2009.02.002.

Losi, G., Knauss, W., 1992. Free volume theory and nonlinear thermoviscoelasticity. Polymer Engineering & Science 32, 542–557. doi:10.1002/pen.760320805.

Minea, A.A., 2021. State of the art in peg-based heat transfer fluids and their suspensions with nanoparticles. Nanomaterials 11, 86.

Mitra, S., Kim, A.R., Zhao, B., Mitra, S.K., 2026. Short-time spreading dynamics of elastic drops. Mater. Adv. 7, 772–782. doi:10.1039/D5MA00896D.

Mkhize, N., Bhaskaran, H., 2022. Electrohydrodynamic jet printing: Introductory concepts and considerations. Small Science 2, 2100073.

Mobaseri, A., Kumar, S., Cheng, X., 2025. Maximum spreading of impacting shear-thinning and shear-thickening drops. Proceedings of the National Academy of Sciences 122, e2500163122. doi:10.1073/pnas.2500163122.

Montgomery, S., Hamel, C., Skovran, J., Qi, H., 2022. A reaction–diffusion model for grayscale digital light processing 3D printing. Extreme Mechanics Letters 53, 101714. doi:10.1016/j.eml.2022.101714.

Moughames, J., Martinez, J.A.I., Ulliac, G., Sylvestre, T., Barbot, A., André, J.C., Qi, H.J., Demoly, F., Kadic, M., 2025. Topology-optimized multimaterial 4d-printed fabry–perot filter with enhanced thermal stability using two-photon polymerization. Thin-Walled Structures 209, 112900.

Mousavi, M., Faroughi, S., 2025. Spreading and rebound of viscoelastic droplets on surfaces with hybrid wettability. Physics of Fluids 37. doi:10.1063/5.0248091.

Odian, G., 2004. Principles of Polymerization. John Wiley & Sons.

Porter, R., Knox, J., Johnson, J., 1968. On the flow and activation energy of branched polyethylene melts. Transactions of the Society of Rheology 12, 409–419. doi:10.1122/1.548925.

Ramesh, S., Mahajan, C., Gerdes, S., Gaikwad, A., Rao, P., Cormier, D.R., Rivero, I.V., 2022. Numerical and experimental investigation of aerosol jet printing. Additive Manufacturing 59, 103090.

Seiti, M., Degryse, O., Ferrraro, R.M., Giliani, S., Bloemen, V., Ferraris, E., 2023. 3d aerosol jet® printing for micro-structuring: Advantages and limitations. International Journal of Bioprinting 9, 57–74.

Sivasankar, V., Sachar, H., Sinha, S., Hines, D., Das, S., 2020. 3d printed microdroplet curing: Unravelling the physics of on-spot photopolymerization. ACS Applied Polymer Materials 2, 966–976. doi:10.1021/acsapm.9b01064.

Smith, M., Bertola, V., 2010. Effect of polymer additives on the wetting of impacting droplets. Physical Review Letters 104, 154502. doi:10.1103/PhysRevLett.104.154502.

Snoeijer, J.H., Pandey, A., Herrada, M.A., Eggers, J., 2020. The relationship between viscoelasticity and elasticity. Proceedings of the Royal Society A: Mathematical, Physical and Engineering Sciences 476, 20200419. doi:10.1098/rspa.2020.0419.

Stansbury, J., Idacavage, M., 2016. 3d printing with polymers: Challenges among expanding options and opportunities. Dental Materials 32, 54–64. doi:10.1016/j.dental.2015.09.018.

Tang, Y., Henderson, C., Muzzy, J., Rosen, D., 2004. Stereolithography cure process modeling using acrylate resin, in: Proceedings of the International Solid Freeform Fabrication Symposium, Austin, TX.

Tomé, M., Mangiavacchi, N., Cuminato, J., Castelo, A., Mckee, S., 2002. A finite difference technique for simulating unsteady viscoelastic free surface flows. Journal of Non-Newtonian Fluid Mechanics 106, 61–106. doi:10.1016/S0377-0257(02)00157-1.

Varma, S.C., Saha, A., Mukherjee, S., Bandopadhyay, A., Kumar, A., Chakraborty, S., 2020. Universality in coalescence of polymeric fluids. Soft Matter 16, 10921–10927. doi:10.1039/D0SM01663B.

Venkatesan, J., Ganesan, S., 2019. Computational modeling of impinging viscoelastic droplets. Journal of Non-Newtonian Fluid Mechanics 263, 42–60. doi:10.1016/j.jnnfm.2018.11.006.

Vlnieska, V., Gilshtein, E., Kunka, D., Heier, J., Romanyuk, Y.E., 2022. Aerosol jet printing of 3d pillar arrays from photopolymer ink. Polymers 14, 3411.

Wang, X., Tian, H., Guo, H., Yan, C., Ran, H., Zhang, R., Wang, C., Li, X., Chen, X., Shao, J., 2024. Droplet volume modulation based on multi-waveform superposition for drop-on-demand material jetting. Additive Manufacturing 79, 103940.

Wang, Y., Do-Quang, M., Amberg, G., 2017. Impact of viscoelastic droplets. Journal of Non-Newtonian Fluid Mechanics 243, 38–46. doi:10.1016/j.jnnfm.2017.02.006.

Webber, D., Orth, A., Vidyapin, V., Zhang, Y., Picard, M., Liu, D., Sampson, K.L., Lacelle, T., Paquet, C., Boisvert, J., 2024. Printing of low-viscosity materials using tomographic additive manufacturing. Additive Manufacturing 94, 104480.

Wu, J., Zhao, Z., Hamel, C., Mu, X., Kuang, X., Guo, Z., Qi, H., 2018. Evolution of material properties during free radical photopolymerization. Journal of the Mechanics and Physics of Solids 112, 25–49. doi:10.1016/j.jmps.2017.11.012.

Yada, S., Bazesefidpar, K., Tammisola, O., Amberg, G., Bagheri, S., 2023. Rapid wetting of shear-thinning fluids. Phys. Rev. Fluids 8, 043302. doi:10.1103/PhysRevFluids.8.043302.

Yoshida, S., Takahata, Y., Horiuchi, S., Kurata, H., Yamamoto, M., 2014. Numerical model of radical photopolymerization based on interdiffusion. International Journal of Polymer Science 2014, 243895. doi:10.1155/2014/243895.

Zarrelli, M., Skordos, A., Partridge, I., 2010. Toward a constitutive model for cure-dependent modulus of a high temperature epoxy during the cure. European Polymer Journal 46, 1705–1712. doi:10.1016/j.eurpolymj.2010.05.002.

Zeng, M., Du, Y., Jiang, Q., Kempf, N., Wei, C., Bimrose, M.V., Tanvir, A., Xu, H., Chen, J., Kirsch, D.J., et al., 2023. High-throughput printing of combinatorial materials from aerosols. Nature 617, 292–298.

Zhang, P., Liu, C., Modavi, C., Abate, A., Chen, H., 2024. Printhead on a chip: empowering droplet-based bioprinting with microfluidics. Trends in Biotechnology 42, 353–368.

Zhao, C., Lee, T., Carlson, A., 2024. Spreading and engulfment of a viscoelastic film onto a newtonian droplet. Phys. Rev. Fluids 9, 094003. doi:10.1103/PhysRevFluids.9.094003.

Zhao, Z., Wu, J., Mu, X., Chen, H., Qi, H., Fang, D., 2017. Desolvation induced origami of photocurable polymers by digit light processing. Macromolecular Rapid Communications 38, 1600625. doi:10.1002/marc.201600625.